University of Reading

On the coupling between barotropic and baroclinic modes of extratropical atmospheric variability

Article

Published Version

Boljka, L., Shepherd, T. G. and Blackburn, M. (2018) On the coupling between barotropic and baroclinic modes of extratropical atmospheric variability. Journal of the Atmospheric Sciences, 75 (6). pp. 1853-1871. ISSN 1520-0469 doi: https://doi.org/10.1175/JAS-D-17-0370.1 Available at http://centaur.reading.ac.uk/75911/

It is advisable to refer to the publisher's version if you intend to cite from the work. See Guidance on citing.

To link to this article DOI: http://dx.doi.org/10.1175/JAS-D-17-0370.1

Publisher: American Meteorological Society

All outputs in CentAUR are protected by Intellectual Property Rights law, including copyright law. Copyright and IPR is retained by the creators or other copyright holders. Terms and conditions for use of this material are defined in the End User Agreement.

www.reading.ac.uk/centaur

University of Reading

CentAUR

Central Archive at the University of Reading

Reading's research outputs online

On the Coupling between Barotropic and Baroclinic Modes of Extratropical Atmospheric Variability

LINA BOLJKA AND THEODORE G. SHEPHERD

Department of Meteorology, University of Reading, Reading, United Kingdom

MICHAEL BLACKBURN

National Centre for Atmospheric Science, University of Reading, Reading, United Kingdom

(Manuscript received 30 November 2017, in final form 2 March 2018)

ABSTRACT

The baroclinic and barotropic components of atmospheric dynamics are usually viewed as interlinked through the baroclinic life cycle, with baroclinic growth of eddies connected to heat fluxes, barotropic decay connected to momentum fluxes, and the two eddy fluxes connected through the Eliassen–Palm wave activity. However, recent observational studies have suggested that these two components of the dynamics are largely decoupled in their variability, with variations in the zonal mean flow associated mainly with the momentum fluxes, variations in the baroclinic wave activity associated mainly with the heat fluxes, and essentially no correlation between the two. These relationships are examined in a dry dynamical core model under different configurations and in Southern Hemisphere observations, considering different frequency bands to account for the different time scales of atmospheric variability. It is shown that at intermediate periods longer than 10 days, the decoupling of the baroclinic and barotropic modes of variability can indeed occur as the eddy kinetic energy at those time scales is only affected by the heat fluxes and not the momentum fluxes. The baroclinic variability includes the oscillator model with periods of 20–30 days. At both the synoptic time scale and the quasi-steady limit, the baroclinic and barotropic modes of variability are linked, consistent with baroclinic life cycles and the positive baroclinic feedback mechanism, respectively. In the quasi-steady limit, the pulsating modes of variability and their correlations depend sensitively on the model climatology.

1. Introduction

The midlatitude dynamics of the Southern Hemisphere (SH) exhibit two distinct so-called annular modes of variability: the southern annular mode (SAM; e.g., Kidson 1988; Hartmann and Lo 1998) and the baroclinic annular mode (BAM; Thompson and Woodworth 2014). The former is based on empirical orthogonal function (EOF) analysis of zonal-mean zonal wind and represents north–south shifts of the jet stream, which are mainly driven by corresponding shifts in eddy momentum fluxes (e.g., Hartmann and Lo 1998; Lorenz and Hartmann 2001). The latter is based on EOF analysis of eddy kinetic energy (EKE) and represents amplitude variations of this field, which are mainly driven by corresponding variations in eddy heat fluxes (Thompson and Woodworth 2014). The SAM has an equivalent barotropic vertical structure and is often referred to as a barotropic mode of variability, whereas the BAM has a stronger vertical structure, as well as being directly linked to heat fluxes, and is therefore related to variability in baroclinic processes.

Thompson and Woodworth (2014) found that the SAM was essentially uncorrelated with eddy heat fluxes, the BAM was essentially uncorrelated with eddy momentum fluxes, and there was only a small (negligible) correlation between the SAM and BAM. These findings led to the conclusion that the eddy momentum and heat fluxes are somewhat independent; hence, there is a decoupling between baroclinic and barotropic modes of variability. This was a somewhat counterintuitive result as the momentum and heat fluxes (and also baroclinic and barotropic processes) are usually viewed as linked through eddy growth and decay in the Eliassen–Palm

Supplemental information related to this paper is available at the Journals Online website: https://doi.org/10.1175/JAS-D-17-0370.s1.

Corresponding author: Lina Boljka, l.boljka@pgr.reading.ac.uk

DOI: 10.1175/JAS-D-17-0370.1

© 2018 American Meteorological Society. For information regarding reuse of this content and general copyright information, consult the AMS Copyright Policy (www.ametsoc.org/PUBSReuseLicenses).

(EP) wave activity perspective (e.g., Simmons and Hoskins 1978; Edmon et al. 1980), and both Robinson (2000) and Lorenz and Hartmann (2001) identified a baroclinic feedback associated with annular-mode anomalies.

However, it is perfectly conceivable to have barotropic variability with fixed baroclinic wave sources (e.g., Vallis et al. 2004). In particular, different momentum fluxes can arise from the same heat fluxes, depending on the upper-tropospheric conditions, as in life cycle 1 (LC1; equatorward wave breaking) and life cycle 2 (LC2; poleward wave breaking) experiments (Thorncroft et al. 1993). Moreover, Pfeffer (1987, 1992) argued that typical aspect ratios implied that heat fluxes mainly act to drive the residual circulation, whereas momentum fluxes mainly drive the zonal-mean-flow tendency, implying irrelevance of heat fluxes for the zonal mean flow. This argument has been formalized in a companion study (Boljka and Shepherd 2018), which, using multiscale asymptotic methods, showed that under such conditions and under synoptic temporal- and spatial-scale averaging, wave activity (generalized eddy kinetic energy) and the vertical component of EP flux (related to heat flux) are indeed related on time scales longer than synoptic and that momentum fluxes do not directly affect this coupling on such time scales.

Thompson and Barnes (2014) further found an oscillator model between EKE and heat flux with a time scale of 20–30 days, which was reflected in the BAM. This model has no influence from the momentum fluxes and is purely baroclinic by nature with a relationship with baroclinicity (vertical wind shear). A similar oscillator model was also found for the Northern Hemisphere in Ambaum and Novak (2014). Such an oscillating relationship is consistent with weakly nonlinear models of baroclinic instability, such as in Pedlosky (1970).

Wang and Nakamura (2015, 2016) also pointed out a relationship between wave activity and heat flux with a similar time scale as in Thompson and Barnes (2014) but only for the SH summer. This suggests that not all seasons exhibit the oscillating behavior (between EKE and heat flux). Wang and Nakamura (2015) further pointed out that momentum and heat fluxes primarily act at different time scales: heat fluxes act primarily at about 20–30-day periods, whereas momentum fluxes act at shorter periods. Wang and Nakamura (2016) investigated the relationship between wave activity and heat fluxes and found that the meridionally confined baroclinic zone in SH summer provides a waveguide that lets different modes interfere and produce larger amplitude heat fluxes with a 20–30-day periodicity.

Here, we look into the behavior discussed above using different configurations of a simplified model and ERA-Interim (described in section 2a). The different model configurations are not intended to realistically mimic the real atmosphere but rather to examine the baroclinic–barotropic coupling across a wide range of dynamical regimes. They also facilitate comparison to previous work done on the baroclinic and barotropic modes of variability using simplified models (e.g., Sparrow et al. 2009; Sheshadri and Plumb 2017). The methods are given in section 2, and the theoretical background in section 3. We first examine in detail one particular (equinox) configuration of the model, in section 4, in order to understand the nature of baroclinic–barotropic interactions on various time scales. In section 5, we assess the generality of our results by comparing them with the winter and summer hemispheres of a solstice configuration of the model and use these findings to interpret the SH behavior seen in ERA-Interim. Conclusions are given in section 6.

2. Methods

a. Data

The numerical model used for this study is the dry dynamical core version of the Met Office Unified Model (UM), version 8.6, with Even Newer Dynamics for General Atmospheric Modelling of the Environment (ENDGame) semi-Lagrangian dynamical core (Walters et al. 2014). The model configuration follows Held and Suarez (1994) with some modifications, being forced through Newtonian relaxation of the temperature field to a prescribed equilibrium profile, with linear frictional and thermal damping. The model resolution used is N96L63 with a model top at 32 km (1.25° in latitude, 1.875° in longitude, and varying vertical resolution—from approximately 200 m in the lower troposphere to approximately 1000 m in the stratosphere) and is run for 10 800 days, of which the first 1440 days are taken as a spinup period. The output is analyzed at daily resolution and in height coordinates.

Two different model configurations were used for this study: (i) the usual Held–Suarez configuration with perpetual equinox conditions as specified in Held and Suarez (1994) and (ii) a stratospheric perpetual solstice configuration, following Polvani and Kushner (2002)'s strong polar vortex forcing ($\gamma = 4$) with a troposphere-to-stratosphere transition at 200 hPa [as used in Sheshadri et al. (2015)]. Note that the tropospheric equilibrium temperature profile was not modified; only the stratospheric profile was. In this configuration, the winter hemisphere (with a strong polar vortex) is in the SH and the summer hemisphere (with a warmer stratosphere) is in the Northern Hemisphere (NH). There is no

orography or other longitudinal asymmetries (such as land–sea contrast) that would give rise to forced stationary planetary waves, and the lack of a seasonal cycle or other sources of external variability means that the model simulations are statistically stationary.

The different model configurations exhibit climatological jets at different latitudes and with different strengths and thereby give rise to different variability. We have three different model climatologies to compare: equinox, winter, and summer. The equinox configuration gives a strong jet centered at 40° (Fig. S1a in the supplementary material), whereas the winter and summer hemispheres of the solstice configuration have weaker jets around 45° and 35° latitude (Figs. S1b and S1c in the supplementary material), respectively.

To test the relationships found in the simplified model in a more realistic setting, the model data are compared to the ERA-Interim observational dataset from the European Centre for Medium-Range Weather Forecasts (Dee et al. 2011). The data are analyzed as daily mean (from four-times-daily resolution—the eddy fluxes are first computed at 6-hourly resolution and then averaged over 24 h) for the time period between 1 January 1981 and 31 December 2010 (10 957 days) on a grid with a resolution of 0.7° in latitude and longitude, and 27 pressure levels between 1000 and 100 hPa. The temporal anomalies were formed by removing the seasonal cycle (subtracting the climatology of each calendar day), hence no specific season is analyzed. Only Southern Hemisphere observed data were analyzed in this study, where the climatological jet is centered around 50° latitude (Fig. S1d in the supplementary material).

b. EOF and regression analysis

EOF analysis is adopted to obtain the leading modes of variability of various fields. The EOF of zonal-mean zonal wind $[u]$ is called SAM, where the dipolar mode (representing shifting of the jet) is called SAM1 (usually the leading mode of variability) and the tripolar mode (representing sharpening and strengthening of the jet) is called SAM2 (usually the second mode of variability). The EOF of EKE ($=0.5[u^{*2} + v^{*2}]$) is called BAM [found in Thompson and Woodworth (2014)], where BAM1 represents the monopolar mode (representing amplitude variations in the EKE field), BAM2 the dipolar mode (representing latitudinal shifts of the field), and BAM3 the tripolar mode (representing sharpening and strengthening of the field). Here, the square brackets represent the zonal mean, the asterisk represents perturbations from the zonal mean, u is zonal velocity, and v is meridional velocity. We recognize that the different EOFs are statistical rather than physically distinct entities, and so they are used only as a basis for our analysis, which focuses on the coupling between barotropic and baroclinic components of the variability.

TABLE 1. Variance explained (%) for the first two SAMs and the first three BAMs for different model configurations and for ERA-Interim under a Lanczos 50-day low-pass filter. Note that the modes are numbered according to spatial structure and not variance explained.

Configuration	SAM1	SAM2	BAM1	BAM2	BAM3
Equinox	84	11	19	70	6
Summer	86	9	24	65	6
Winter	59	31	32	42	13
ERA-Interim	59	25	38	23	14

Additional modes of variability are defined based on eddy momentum fluxes (EMFs; $[v^*u^*]$) and eddy heat fluxes (EHFs; $[v^*\theta^*]$), where θ is potential temperature. Here, EMF1 and EHF1 are monopolar modes (representing amplitude variations), EMF2 and EHF2 are dipolar modes (representing latitudinal shifts), and EHF3 is a tripolar mode (representing sharpening and strengthening of the field). Note that the modes are numbered according to their spatial structure and not by the variance explained; hence, in some cases the leading modes can be SAM2, BAM2, etc. (as shown in Table 1).

Before calculating the EOFs of the fields, a mass-weighted vertical average is applied to the zonal-mean model fields in height coordinates:

$$\langle T \rangle = \frac{\sum_{k=0}^{N} [\rho T]_k \, (z_{k+1/2} - z_{k-1/2})}{\sum_{k=0}^{N} [\rho]_k \, (z_{k+1/2} - z_{k-1/2})}, \tag{1}$$

where T is the zonally averaged field of interest, ρ is density, angle brackets represent the vertical average, k represents the vertical levels of the given quantity, $k \pm 1/2$ represents the half levels (vertical levels between k levels), N is the top vertical level of interest, and z is the vertical coordinate. For ERA-Interim, a pressure-weighted vertical average is applied: $\langle T \rangle = p_o^{-1} \sum_{k=0}^{N} [T]_k \, (p_{k-1/2} - p_{k+1/2})$, where p is pressure and $p_o = \sum_{k=0}^{N} (p_{k-1/2} - p_{k+1/2})$. The vertical average is taken from the surface up to 11.5 km (200 hPa for ERA-Interim) except for heat flux where 5 km (500 hPa for ERA-Interim) was used since θ increases rapidly with height. Thus, only tropospheric variability is represented in these diagnostics. These vertically averaged fields, weighted by $\sqrt{\cos\phi}$, are then used to calculate EOFs of zonal-mean zonal wind, EKE, and eddy heat and eddy momentum flux.

TABLE 2. Correlation between SAM1 and BAM2 at lag 0 for different model configurations and for ERA-Interim for unfiltered and low- and high-pass filtered data. Only statistically significant correlations (exceeding the 95% threshold) are given.

Configuration	Unfiltered	Low pass	High pass
Equinox	0.45	0.87	−0.55
Summer	0.62	0.92	−0.55
Winter	0.29	0.66	−0.31
ERA-Interim	−0.05	0.63	−0.28

After calculating the EOFs, various fields are regressed onto the principal components (PCs) of these modes of variability. The regressed fields include zonal-mean zonal wind, EKE, and eddy heat and eddy momentum flux. These show the relationship between the different dynamical fields involved in each mode of variability as well as identify the leading modes of variability in terms of their spatial structure. The correlations between different PC time series of SAMs and BAMs of variability are given in Tables 2–4 and are discussed later in context.

For reference, the contours in Fig. 1 show regressions of zonal-mean zonal wind on SAM1 and SAM2; of EKE on BAM1, BAM2, and BAM3; of momentum flux on EMF1 and EMF2; and of heat flux on EHF1, EHF2, and EHF3 for the model equinox configuration using unfiltered data and without any time lags. The colors in the figures show the climatologies of the regressed fields. The horizontal pairing of panels reflects the dominant relationships between modes (e.g., SAM1 has a clear relationship with EMF1 through the zonal momentum equation). The figure illustrates the typical spatial structures that these modes have, as described above.

c. *Power spectrum, temporal filtering, and cross-spectrum analysis*

To calculate the power spectra of the PC time series of the EOF fields (e.g., SAM, BAM, EHF, EMF), we follow the methodology used in Byrne et al. (2016). The data are first windowed using a Hanning window, then a periodogram is calculated, and finally, the fields are smoothed using Daniell filters following Bloomfield (2000).

These power spectra (based on unfiltered data) were used to determine the frequency bands at which different dynamical processes take place (section 4). The original data (not PC time series) were then filtered according to the frequency bands using the Lanczos filter (Duchon 1979), and EOFs were recalculated from the filtered data. Note that the EKE, heat flux, and momentum flux time series are filtered, not each component of them separately (e.g., u, v, θ) as we are interested in the wave–mean flow interaction on different time scales rather than in which waves (low or high frequency) contribute to the behavior.

TABLE 3. As in Table 2, but for SAM2 and BAM1.

Configuration	Unfiltered	Low pass	High pass
Equinox	−0.28	—	−0.53
Summer	−0.34	0.07	−0.57
Winter	−0.32	−0.65	−0.27
ERA-Interim	−0.31	−0.42	−0.29

The cross-spectrum analysis was computed following Lorenz and Hartmann (2001). We first obtained the relevant unfiltered time series (section 3), and then we divided them into 256- and 512-day sections (for comparison) overlapped by 128 and 256 days, respectively, and windowed each section by a Hanning window. These gave at least 72 and 36 degrees of freedom, respectively. The cross spectra of each section were then averaged and smoothed using Daniell filters (as for the power spectra).

3. Theoretical background

Wave–mean flow interactions are usually studied using the zonal momentum budget and EP wave activity theory, and the transformed Eulerian mean (TEM) perspective (Andrews and McIntyre 1976) yields a direct link between the two quantities. However, the BAMs are based on EKE. While EKE may be considered a proxy for EP wave activity, there is also an EKE equation derivable within the TEM framework, which in log pressure coordinates is (Plumb 1983)

$$\frac{\partial[K_E]}{\partial t} = C(P_E \to K_E) - C(K_E \to K_M) - \frac{1}{p_{\ln}}\nabla\cdot\mathbf{B}(K_E) + S(K_E), \tag{2}$$

where

$$C(P_E \to K_E) = \frac{Rp_{\ln}^{\kappa}}{H}\frac{[\mathbf{u}^*\theta^*]\cdot\nabla[\theta]}{\partial[\theta]/\partial z_{\ln}} \tag{3}$$

represents the conversion from eddy potential energy P_E to EKE K_E, $C(K_E \to K_M) = p_{\ln}^{-1}[u]\nabla\cdot\mathbf{F}$ represents the conversion from EKE K_E to zonal-mean kinetic energy K_M, $\mathbf{B}(K_E) = p_{\ln}[\mathbf{u}^*\phi^*] + [u]\mathbf{F}$ is the EKE flux term, and $S(K_E) = [\mathbf{u}^*\cdot\mathbf{L}^*]$ is the source–sink term of EKE. Here,

$$\mathbf{F} = p_{\ln}\left\{-[u^*v^*], \frac{f[v^*\theta^*]}{\partial[\theta]/\partial z_{\ln}}\right\}$$

is the quasigeostrophic (QG) EP flux (its divergence represents the eddy torque on the mean flow),

TABLE 4. As in Table 2, but for SAM2 and BAM3.

Configuration	Unfiltered	Low pass	High pass
Equinox	0.30	0.81	0.03
Summer	0.32	0.75	—
Winter	0.27	0.50	0.04
ERA-Interim	0.05	0.27	0.09

$\nabla = (\partial/\partial y, \partial/\partial z_{\ln})$, $p_{\ln} = \text{Pressure}/1000\,\text{hPa}$, $z_{\ln} = -H \ln p_{\ln}$ is log pressure vertical coordinate, $\kappa = R/c_p$, R is gas constant, c_p is specific heat at constant pressure, y represents latitude, $\mathbf{L}$ is frictional force, ϕ is geopotential, $\mathbf{u} = (u, v, w)$ is velocity vector, H is a constant scale height (approximately 10 km), and f is the Coriolis parameter.

Simplified TEM equations

Lorenz and Hartmann (2001) used cross-spectrum analysis to show that the vertically averaged zonal-mean zonal wind ($z_u = \langle [u] \rangle$) and eddy momentum flux convergence $\{m = -\partial_y (\langle \rho_o [u^* v^*] \rangle)$ with $\partial_y = \partial/\partial y$ and ρ_o the vertical density profile$\}$ were linearly related according to

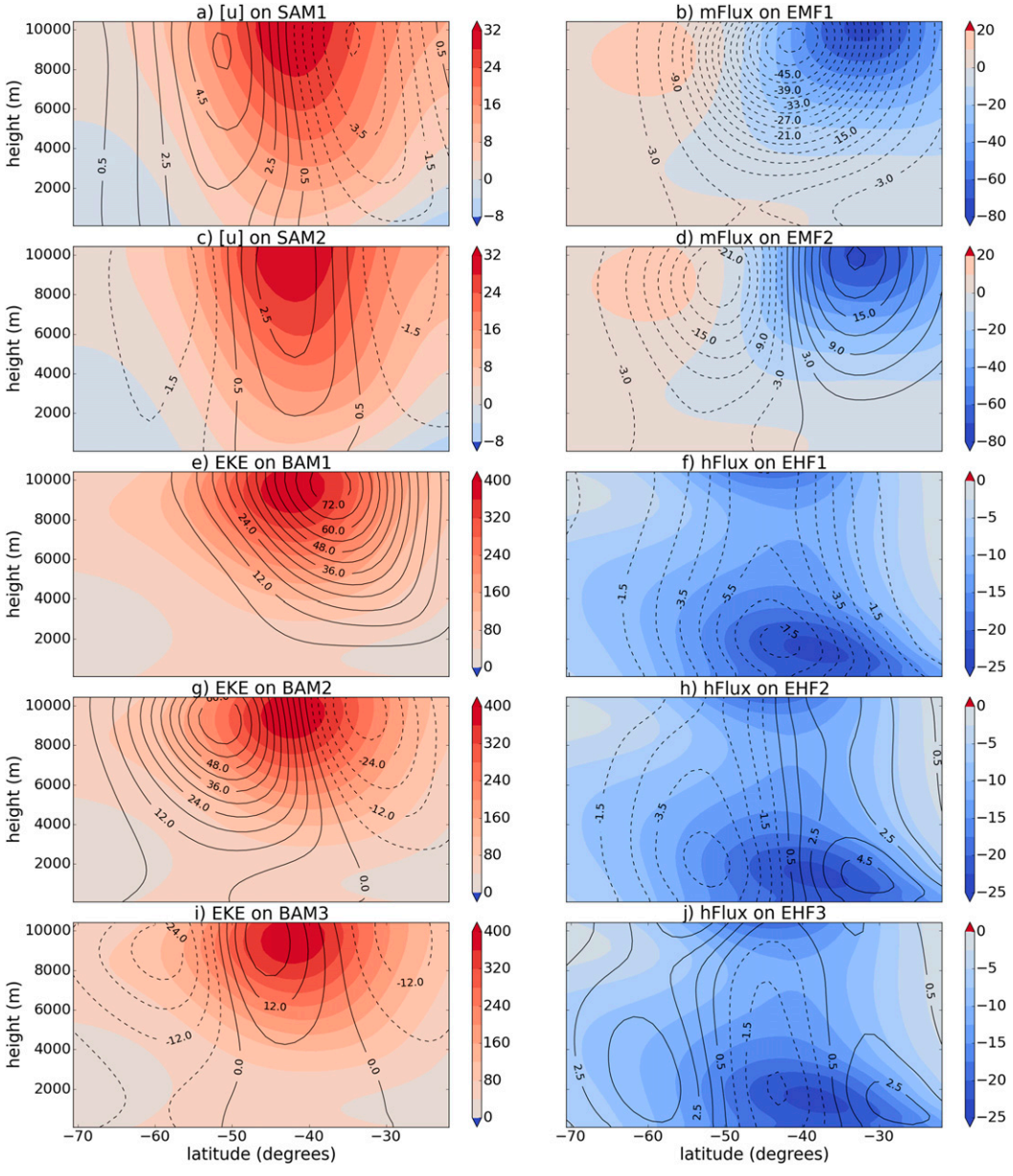

FIG. 1. Contours show regressions of zonal-mean zonal wind $[u]$ on (a) SAM1 and (c) SAM2 (contour interval is 1 m s^{-1}); of EKE on (e) BAM1, (g) BAM2, and (i) BAM3 (contour interval is 6 m^2 s^{-2}); of momentum flux $[u^* v^*]$ on (b) EMF1 and (d) EMF2 (contour interval is 3 m^2 s^{-2}); and of heat flux $[v^* \theta^*]$ on (f) EHF1, (h) EHF2, and (j) EHF3 (contour interval is 1 m K s^{-1}). Colors show the climatologies of the regressed fields. Data are from the equinox model configuration and were not filtered.

$$\frac{\partial z_u}{\partial t} = m - \frac{z_u}{\tau}, \tag{4}$$

with τ a constant. This relationship follows from the zonal momentum equation under QG scaling provided the source–sink term can be represented as a linear damping $-z_u/\tau$ (dominated by boundary layer friction). As discussed by Boljka and Shepherd (2018), the relationship between m and $\partial z_u/\partial t$ is only approximate, since planetary-scale heat fluxes also contribute to angular momentum via meridional mass redistribution, but the latter are negligible in QG scaling (Haynes and Shepherd 1989). Applying a spectral analysis (Fourier transform) yields a cross-spectrum relationship (Lorenz and Hartmann 2001):

$$\frac{\overline{Z}M}{\overline{Z}Z} = i\omega + \frac{1}{\tau} \tag{5}$$

where Z and M represent the Fourier transforms of z_u and m, respectively, the overbar denotes the complex conjugate, and ω is the angular frequency. The value of τ is determined by finding an empirical linear regression to the cross-spectrum [as described in appendix A of Lorenz and Hartmann (2001)]

$$\frac{\overline{Z}M}{\overline{Z}Z} = \beta + i\vartheta\omega,$$

from which $\tau = \vartheta/\beta$.

The relationship (5) suggests that the real part of the cross-spectrum $\overline{Z}M/\overline{Z}Z$ is constant (τ^{-1}), while the imaginary part of the cross spectrum changes linearly with ω. This is illustrated in section 4.

Thompson and Woodworth (2014) and Thompson and Barnes (2014) suggested there existed a relationship between EKE and heat flux independent of momentum flux convergence or zonal-mean zonal wind. Thompson et al. (2017) hence suggested a relationship between EKE and heat flux that is similar to (4), namely,

$$\frac{\partial [K_E]}{\partial t} = \alpha_{\mathrm{EKE}}[v^*\theta^*] - \frac{[K_E]}{\tau_{\mathrm{EKE}}}, \tag{6}$$

where $|\alpha_{\mathrm{EKE}}| \approx 3 \times 10^{-5}\,\mathrm{m\,K^{-1}\,s^{-2}}$ and $\tau_{\mathrm{EKE}} \approx 3$ days are constants, EKE is taken at 300 hPa, heat flux is taken at 850 hPa, and both quantities were averaged meridionally between 40° and 60° latitude where EKE peaks (in ERA-Interim data). Thompson et al. (2017) found that such a simple model reproduced the oscillator model of Thompson and Barnes (2014); thus, we test this relationship using cross-spectrum analysis to see how well it holds at different time scales. The cross-spectrum relationship corresponding to (6) is

$$\alpha_{\mathrm{EKE}}\frac{\overline{E}H}{\overline{E}E} = i\omega + \frac{1}{\tau_{\mathrm{EKE}}}, \tag{7}$$

where E and H now represent Fourier transforms of EKE and heat flux, respectively. In contrast to (5), there is now an empirical factor α_{EKE} [since (6) is not exact], which is determined by finding a linear regression to $\overline{E}H/\overline{E}E$ at frequencies lower than 0.1 cycles per day (cpd) so that the imaginary part of $\alpha_{\mathrm{EKE}}\overline{E}H/\overline{E}E$ is proportional to ω.

Equation (6) is simplified compared to the TEM EKE equation [(2)], only representing $C(P_E \rightarrow K_E)$ [(3)] explicitly (assuming $[v^*\theta^*] \propto [v^*\theta^*]$, which is valid under QG scaling), with the other terms subsumed in the linear damping term. Although latitudinal averaging will eliminate the EKE flux component of (2), it will not eliminate the $C(K_E \rightarrow K_M)$ term unless $[u]$ is slowly varying compared to $\nabla \cdot \mathbf{F}$, which is not the case. In this respect, the wave activity equation is much cleaner (Wang and Nakamura 2015, 2016). Our approach here is not to justify the approximation (6) but rather to examine how well it holds across time scales as a way of understanding the observed BAM–SAM decoupling. Based on the analysis of Boljka and Shepherd (2018), we expect that (in addition to latitudinal averaging) the relationship (6) would only hold at time scales longer than synoptic (and not necessarily at quasi-steady states), which is also tested below.

4. Equinox results

a. Cross spectra

Lorenz and Hartmann (2001) have shown in observations that cross-spectrum analysis [see (5)] supports the relationship between vertically averaged zonal-mean zonal flow and eddy momentum flux convergence described by (4). Indeed, Fig. 2a shows that these two quantities are related in the equinox model configuration at all frequencies as the real part of the cross spectrum is constant and proportional to τ^{-1} with $\tau \approx 10.6$ days, and the imaginary part of the cross spectrum nicely follows the ω slope. Figure 2b shows that the phase difference between m and z_u at low frequencies is small (they are in phase), whereas at the highest frequencies, corresponding to synoptic time scales of 5–10 days, they are nearly 90° out of phase. These two figures thus clearly illustrate that at very low frequencies, $z_u/\tau \approx m$, whereas at the highest frequencies, $\partial z_u/\partial t \approx m$, as expected from (4).

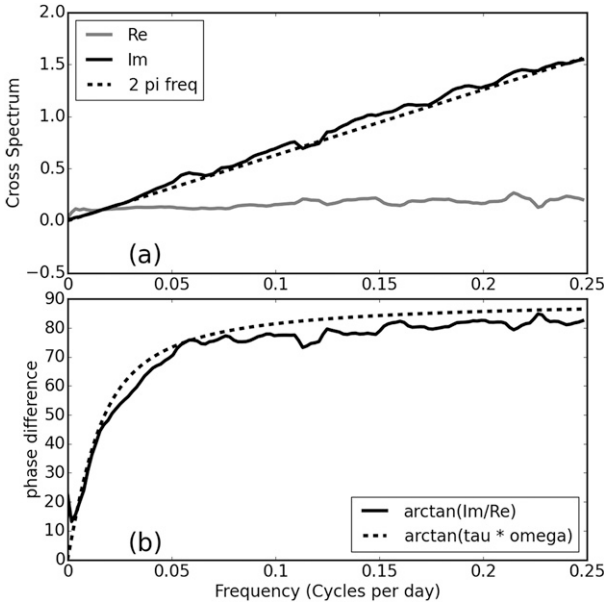

FIG. 2. Imaginary and real parts of (a) cross spectrum and (b) phase difference between zonal-mean zonal wind Z and eddy momentum flux convergence M. Data were split into 512-day-long segments overlapped by 256 days. Vertically averaged (full depth) momentum flux convergence was regressed onto EOF1 of $[u]$ to obtain time series. Data are from the equinox model configuration and were not filtered. Note that a similar figure can be obtained for EOF2 of $[u]$.

In section 3, we presented a simplified theory for the EKE budget in (6) and (7), which is analogous to Lorenz and Hartmann (2001)'s approximation for the zonal momentum equations [(4) and (5)]. Here, we test this theory using cross-spectrum analysis [(7)] after averaging over different latitudinal bands.

First, we test the relationship for a 20° latitudinal band (EKE taken at 9000 m, heat flux at 1500 m, and both averaged between 30° and 50° latitude where both quantities peak; Figs. 1e–j; color shading) for the equinox model configuration, using different lengths of segments: 256 and 512 (Fig. 3). In general, for both lengths of segments, the relationship holds well at frequencies lower than 0.1 cpd, above which the imaginary part of the cross spectrum becomes constant with frequency or even decreases, while the real part of the cross spectrum remains reasonably constant. Different segment lengths show that the peaks apparent at synoptic time scales are reasonably random and that noise increases as longer segments are taken because of fewer degrees of freedom and finer frequency resolution. The value of $|\alpha_{\mathrm{EKE}}|$ varies between 7 and 8.5 $\times$ $10^{-5}\,\mathrm{m\,K^{-1}\,s^{-2}}$, and τ_{EKE} varies between 2.5 and 4.2 days. The poor approximation at synoptic time scales suggests that at these time scales the other terms in (2) (such as momentum fluxes and

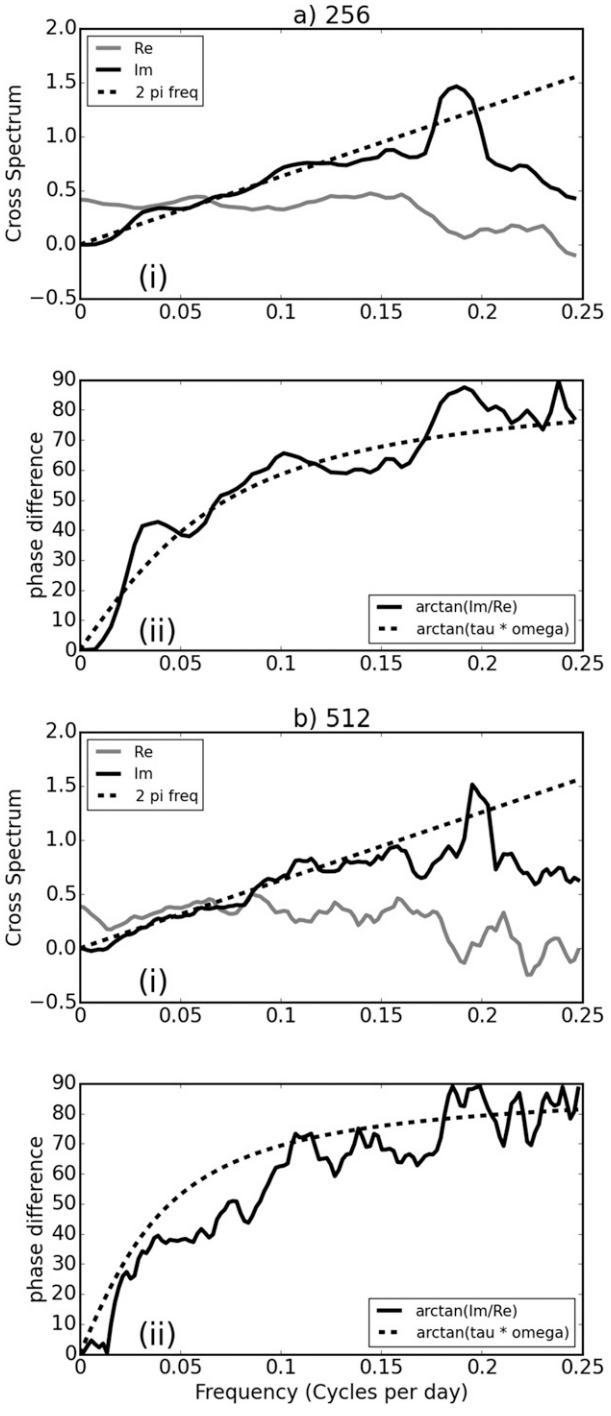

FIG. 3. [a(i)],[b(i)] Imaginary and real parts of cross spectrum and [a(ii)],[b(ii)] phase difference between EKE E and eddy heat flux H for data split into (a) 256- and (b) 512-day-long segments overlapped by a half length. EKE was taken at 9000 m, and heat flux was taken at 1500 m. Both were averaged between 30° and 50°S. Data are from the equinox model configuration and were not filtered.

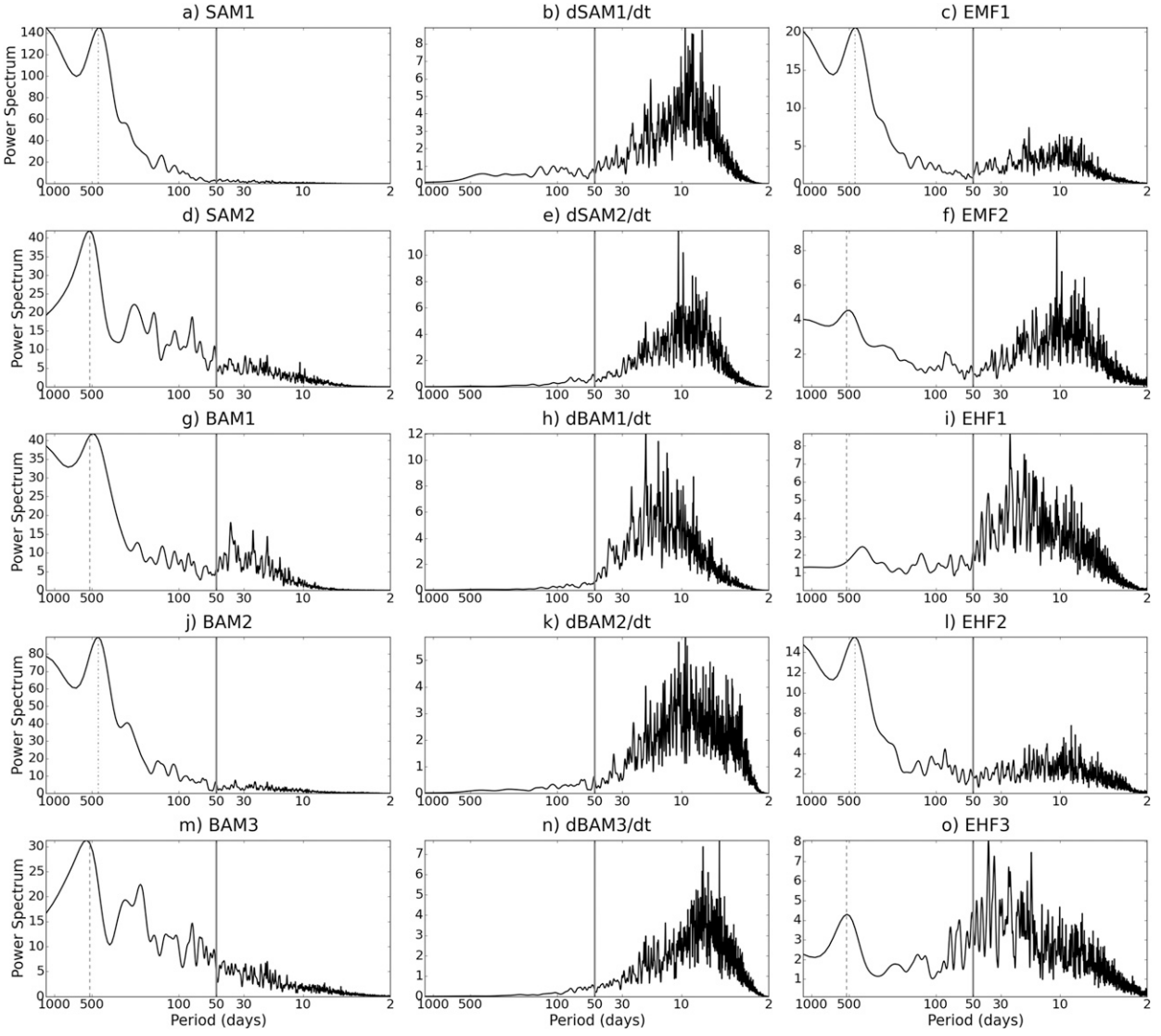

FIG. 4. Power spectra (day^{-1}) of unfiltered PC time series of different fields as labeled. Refer to the text for description of modes; see also Fig. 1. Vertical gray dash–dotted and dashed lines indicate the main peaks in SAM1 and SAM2 power spectra, respectively, and the gray solid line indicates the frequency cutoff used later for filtering. Data are from the equinox model configuration.

EKE fluxes) indeed matter. Nonetheless, Fig. 3 shows that such a simple relationship holds reasonably well at periods longer than 10 days. This is consistent with the prediction of the multiscale asymptotic theory of Boljka and Shepherd (2018), after averaging over synoptic time and spatial scales. Similar results can be obtained also with 10° and 90° latitudinal bands (not shown), which means that the relationship is robust for latitudinal averages of 10° and wider. This is consistent with Wang and Nakamura (2015, 2016).

Note that the real and imaginary parts of the cross spectra cross at a higher frequency than for the momentum flux convergence and zonal-mean zonal wind, because of the damping time scale τ_{EKE} being significantly smaller than τ, implying stronger baroclinic damping processes compared to the barotropic ones. Consequently, the phase difference [Figs. 3a,b(ii)] increases more gradually than for the barotropic processes (Fig. 2b) and by frequency 0.25 cpd reaches just below 80°. This suggests that the quasi-steady relationship $[K_E]/\tau \approx \alpha_{\mathrm{EKE}}[v^*\theta^*]$ holds down to periods of about 20 days for EKE and heat flux, whereas for momentum flux convergence and zonal-mean zonal wind, it only holds at periods longer than about 50 days. We thus consider the low-frequency range with periods longer than 50 days to be in a quasi-steady balance.

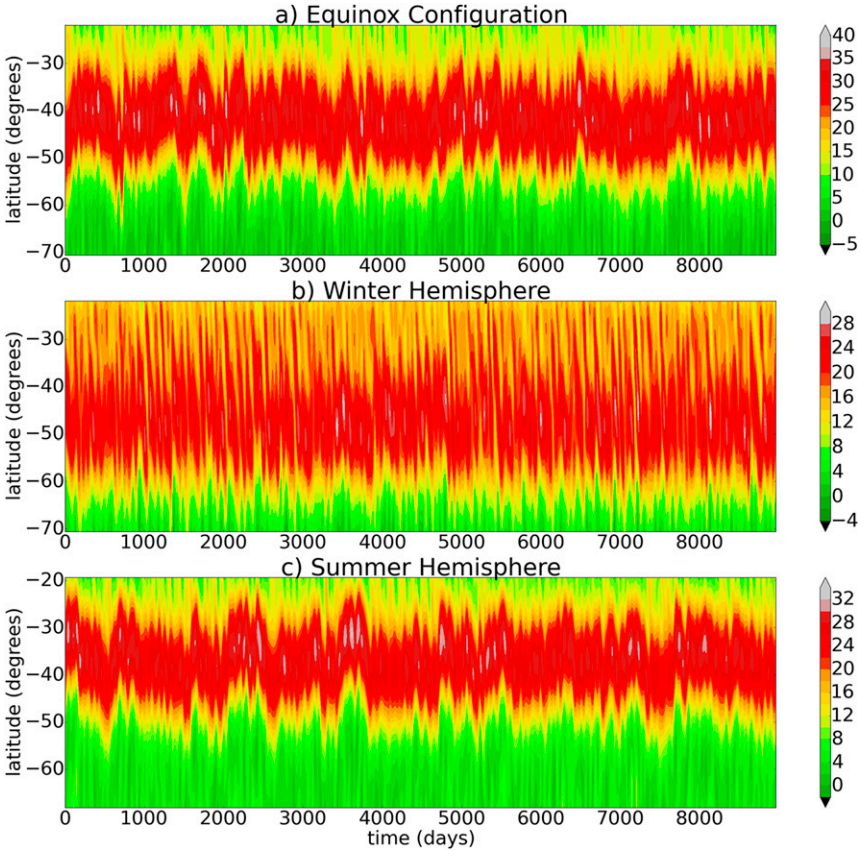

FIG. 5. Low-pass zonal-mean zonal wind [u] time series at 10 km for different model setups: (a) equinox, (b) winter hemisphere, and (c) summer hemisphere model configurations. Note that the summer hemisphere data were plotted as SH for easier comparison with other configurations.

b. *Power spectra*

Power spectra for the model equinox configuration are calculated for the PC time series of EOF fields (SAM, BAM, EHF, and EMF) for the first two or three modes of variability in Fig. 4. The frequency spectra for the tendency of SAM and BAM are also shown as these two modes show mainly low-frequency behavior, whereas their tendencies reflect the higher-frequency behavior as well. This is clearly shown in Fig. 4, where SAM1, SAM2, BAM2, and BAM3 show predominantly low-frequency behavior with the highest peaks well beyond 50 days, whereas their tendencies show higher-frequency behavior on synoptic time scales with continuous spectra peaked around 10 days. These spectra suggest that at lower frequencies, zonal-mean zonal wind and EKE are related to the eddy fluxes (the lower-frequency part of the EMF1, EMF2, EHF2, and EHF3 spectra), whereas at higher frequencies, it is rather their tendencies that are related to the eddy fluxes (the higher-frequency part of the EMF1, EMF2, EHF2, and EHF3 spectra), distinguishing the different behavior anticipated from (4) and (6).

The power spectrum for BAM1 instead has a high-frequency peak around a 40-day period and has another peak at lower frequencies, while its tendency shows a continuous spectrum peaked around a 20-day period. This suggests that the lower- and higher-frequency behaviors (reflected in EKE and in the tendency of EKE) for BAM1 are not well separated and overlap in the frequency domain, in contrast to the other modes. EHF1 and the tendency of BAM1 both show a distinct peak at about the 20–30-day period, which is consistent with the results of Thompson and Barnes (2014) and Wang and Nakamura (2015), who found an oscillatory behavior between EKE (or wave activity) and heat flux with similar periods. The spectra suggest that this oscillatory behavior at these periods is distinct.

From the power spectra, a frequency cutoff can be determined for the high-pass and low-pass filtering. The thick solid gray line in Fig. 4 shows the chosen cutoff period of 50 days, which distinguishes between the distinct behaviors in the two frequency bands (i.e., low

pass includes periods longer than 50 days and high pass includes periods shorter than 50 days). Note that the cutoff period of 30 days that was used in previous studies (e.g., Sparrow et al. 2009) would not be a good choice here. While the low-pass data represent modes of variability in quasi-steady balance, the high-pass data include both synoptic time-scale variability and intermediate time scales (time scales longer than synoptic and shorter than quasi-steady balance), where both the time tendency and linear damping terms in (4) and (6) are nonnegligible.

It is clear from the power spectra that higher frequencies overlap and it is hard to separate the high-frequency behavior of EHF1 and BAM1 from that of EHF2, EHF3, EMF1, EMF2, BAM2, BAM3, SAM1, or SAM2 from the power spectra alone. However, at low frequencies, there are distinct spectral peaks. Because the model setup is statistically stationary, these spectral peaks presumably arise from a limited sampling of red-noise variability. We can use this feature to our advantage, because it provides a clear fingerprint of covariability when the peaks match between different quantities. While the peaks themselves are not robust to subsampling (e.g., Fig. S2 in the supplementary material), all of the conclusions below are robust to subsampling, and indeed, that robustness provides more confidence in the presented results.

The dash–dotted and dashed lines in Fig. 4 show the peaks in the SAM1 and SAM2 power spectra, respectively, for periods between 50 and 1000 days. To be identified, the peaks had to be separated by at least 10 data points (with frequency resolution of $1/9360\,\mathrm{day}^{-1}$) and had to be higher than 5/6 of the maximum value in the low-frequency part of the spectrum. The SAM1 peaks were then projected on the BAM2, EHF2, and EMF1 panels, whereas the SAM2 peaks were projected on the BAM1, BAM3, EHF1, EHF3, and EMF2 panels to locate matching peaks. If the main peaks approximately match, then this provides prima facie evidence for a relation between the modes. For the model equinox configuration, this shows a clear low-frequency relation between SAM1, EMF1, BAM2, and EHF2. The relations between SAM1 and EMF1 and between BAM2 and EHF2 reflect the quasi-steady limit of (4) and (6) (i.e., $z_u/\tau \approx m$ and $[K_E]/\tau_{\mathrm{EKE}} \approx \alpha_{\mathrm{EKE}}[v^*\theta^*]$), but the cross relation between SAM1 and BAM2 is nontrivial. The strong positive correlation for low-pass data is shown in the top row of Table 2. Similarly, there is a different low-frequency relation between SAM2, EMF2, BAM3, and EHF3, pointing to a nontrivial relation between SAM2 and BAM3. The strong positive correlation for low-pass data is shown in the top row of Table 4. The link between any of these modes and BAM1 or EHF1 is weaker (see also top row of Table 3).

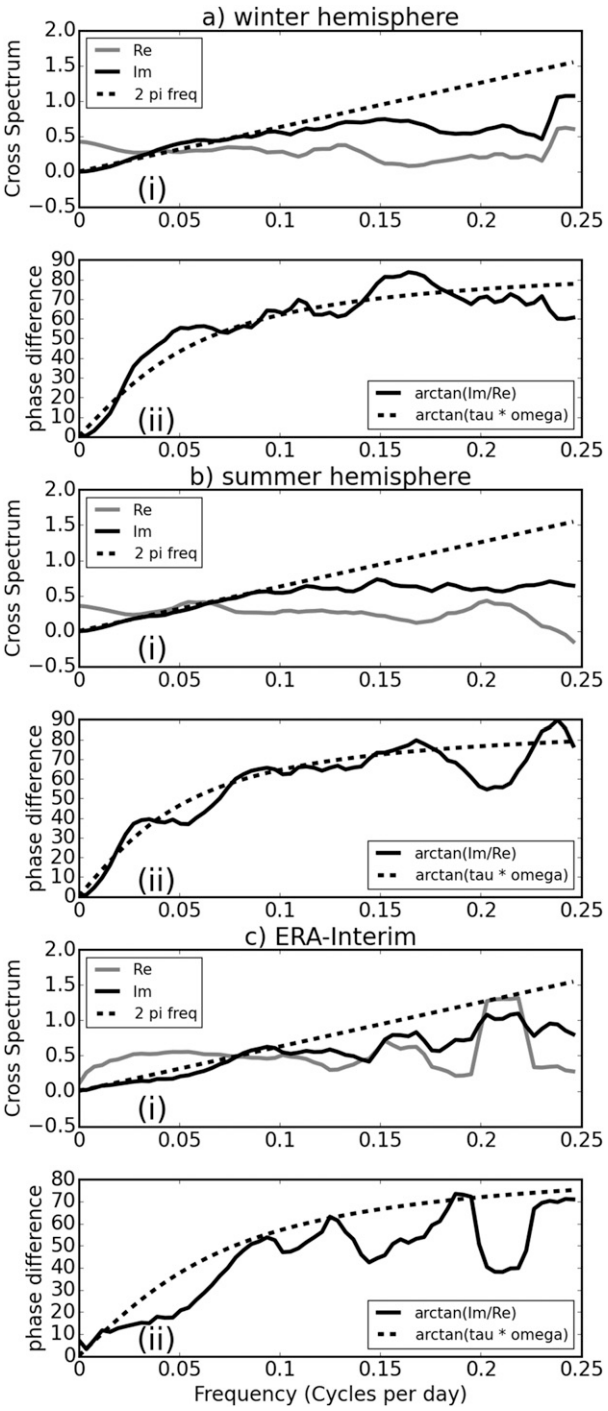

FIG. 6. [a(i)],[b(i)] Imaginary and real parts of cross spectrum and [a(ii)],[b(ii)] phase difference between unfiltered EKE E and eddy heat flux H for (a) winter hemisphere, (b) summer hemisphere, and (c) ERA-Interim. Data were split into 256-day-long segments overlapped by 128 days. EKE was taken at 9000 m (300 hPa for ERA-Interim) and heat flux was taken at 1500 m (850 hPa for ERA-Interim); both were averaged between (a) 35° and 55°, (b) 25° and 45°, and (c) 40° and 60° latitudes.

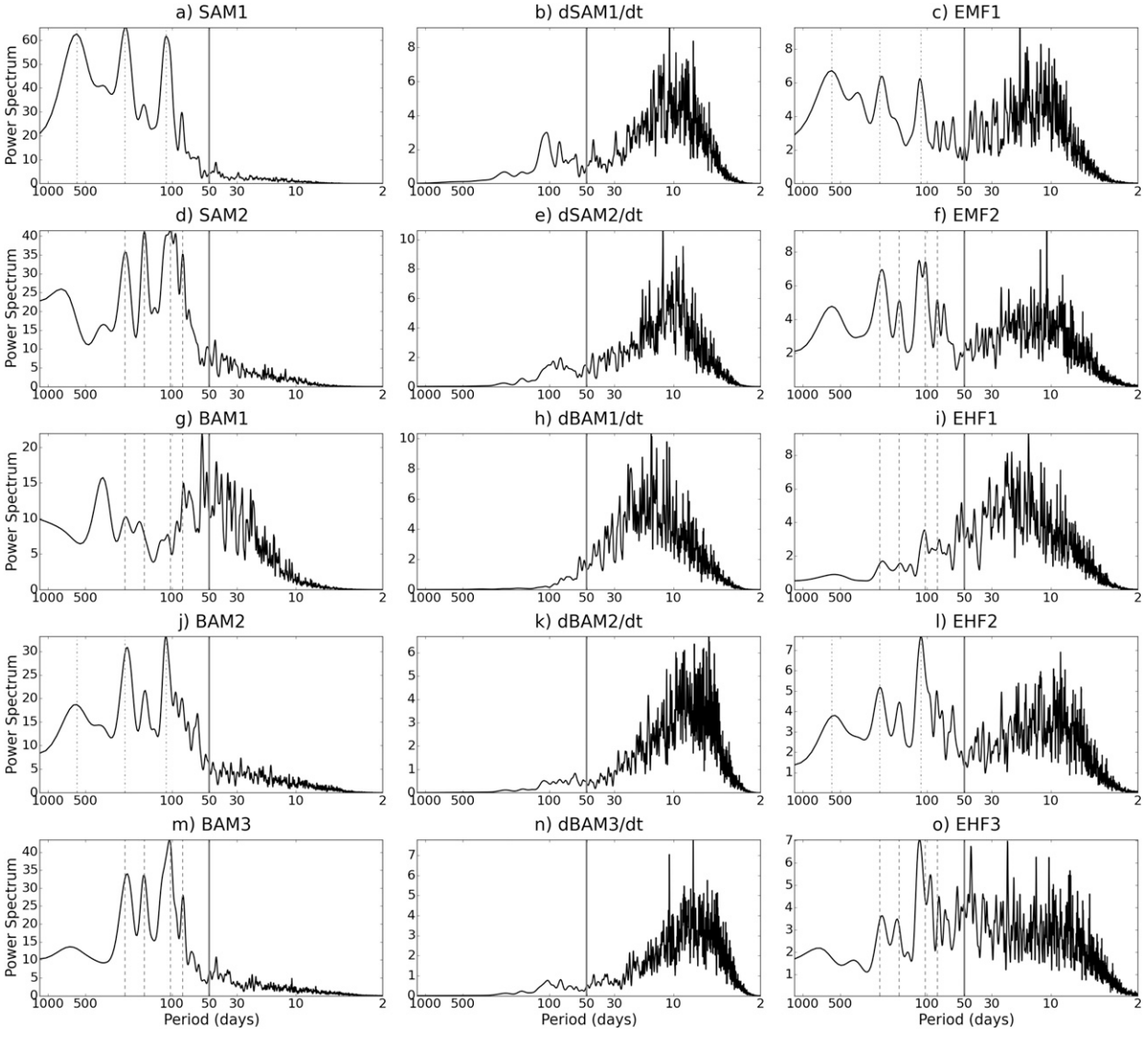

FIG. 7. As in Fig. 4, but for the winter hemisphere model configuration.

Therefore, we find no evidence of a quasi-steady cross-mode relationship between SAM1 and BAM1, which was the correlation examined (using unfiltered data) by Thompson and Woodworth (2014). Note that the correlations shown in Tables 2–4 are robust to subsampling; that is, high correlations are robustly high and small or non-robust correlations are consistently small or nonrobust.

These power spectra and correlations thus reveal three main mechanisms:

- The Thompson and Woodworth (2014) and Thompson and Barnes (2014) picture of a relationship between BAM1 and EHF1 through the oscillator model, with periods of 20–30 days (intermediate time scale)
- The classical (quasi steady) positive baroclinic feedback picture (e.g., Robinson 2000) where the storm tracks move with the jet shifts (this feedback is possible if the eddies are absorbed at a different latitude than their source region), which is reflected in the positive correlations at low frequencies between SAM1 and BAM2/EHF2, and between SAM2 and BAM3/EHF3, and in the regressions of EKE on low-frequency SAM1 and SAM2 (see next section)
- The higher-frequency (synoptic time scale) picture of transient wave–mean flow interaction (e.g., Edmon et al. 1980), in which SAM1, SAM2, EMF1, EMF2, BAM2, BAM3, EHF2, and EHF3 all show power peaking around 10 days and there are negative correlations (at zero lag) in high-pass data between SAM1 and BAM2 (see further discussion in section 5).

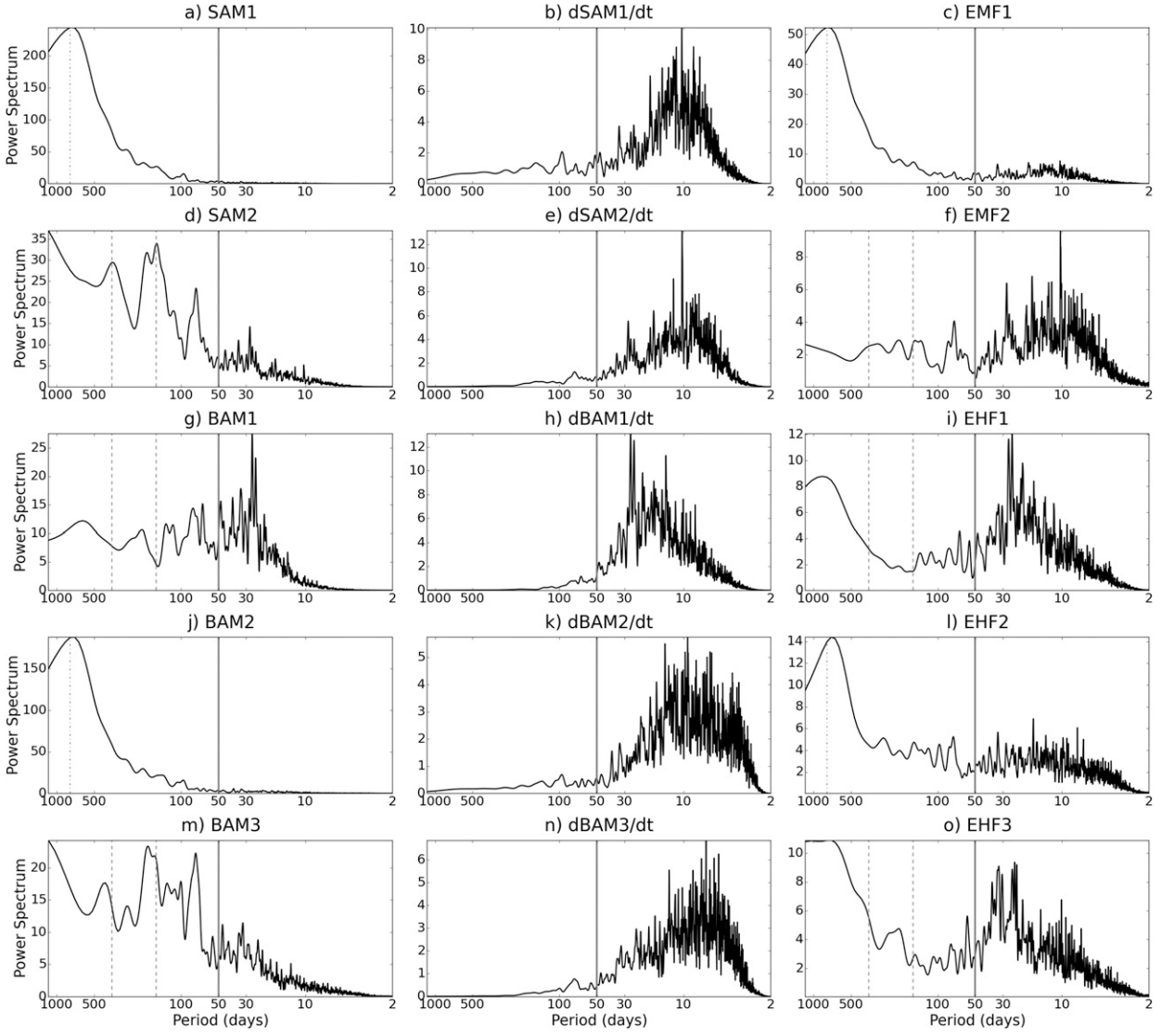

FIG. 8. As in Fig. 4, but for the summer hemisphere model configuration.

5. Comparison to other model configurations and to SH observations

The results from the equinox model configuration are now compared to the summer and winter hemispheres of the solstice model configuration, as well as to the SH in ERA-Interim. This is important as the different model configurations can exhibit different variability because of different climatologies. Figure 5 shows the low-pass zonal-mean zonal wind time series at 10 km for the different model configurations. It is clear that the summer and equinox configurations exhibit more persistence in their jet variability compared with the winter configuration. In particular, the shifting modes (SAM1, BAM2) in these two configurations show a clear dominance over the rest of the modes (Table 1).

Figure 6 shows the EKE and eddy heat flux cross-spectrum analysis for the winter (Fig. 6a) and summer (Fig. 6b) model configurations, and for ERA-Interim (Fig. 6c). These, together with Fig. 3a, show the robustness of relationship (6) between EKE and eddy heat flux for periods longer than 10 days and for an average over a few latitudinal bands. (A 10° average is sufficient, but the signal is stronger for a 20° average; hence, the former was omitted for brevity.) This is consistent with the decoupling of baroclinic and barotropic modes of variability under synoptic-scale averaging [as predicted by Boljka and Shepherd (2018)] and is robust for all model configurations and for ERA-Interim (i.e., independent of setting), in the sense that the momentum fluxes are not needed to account for EKE variability at

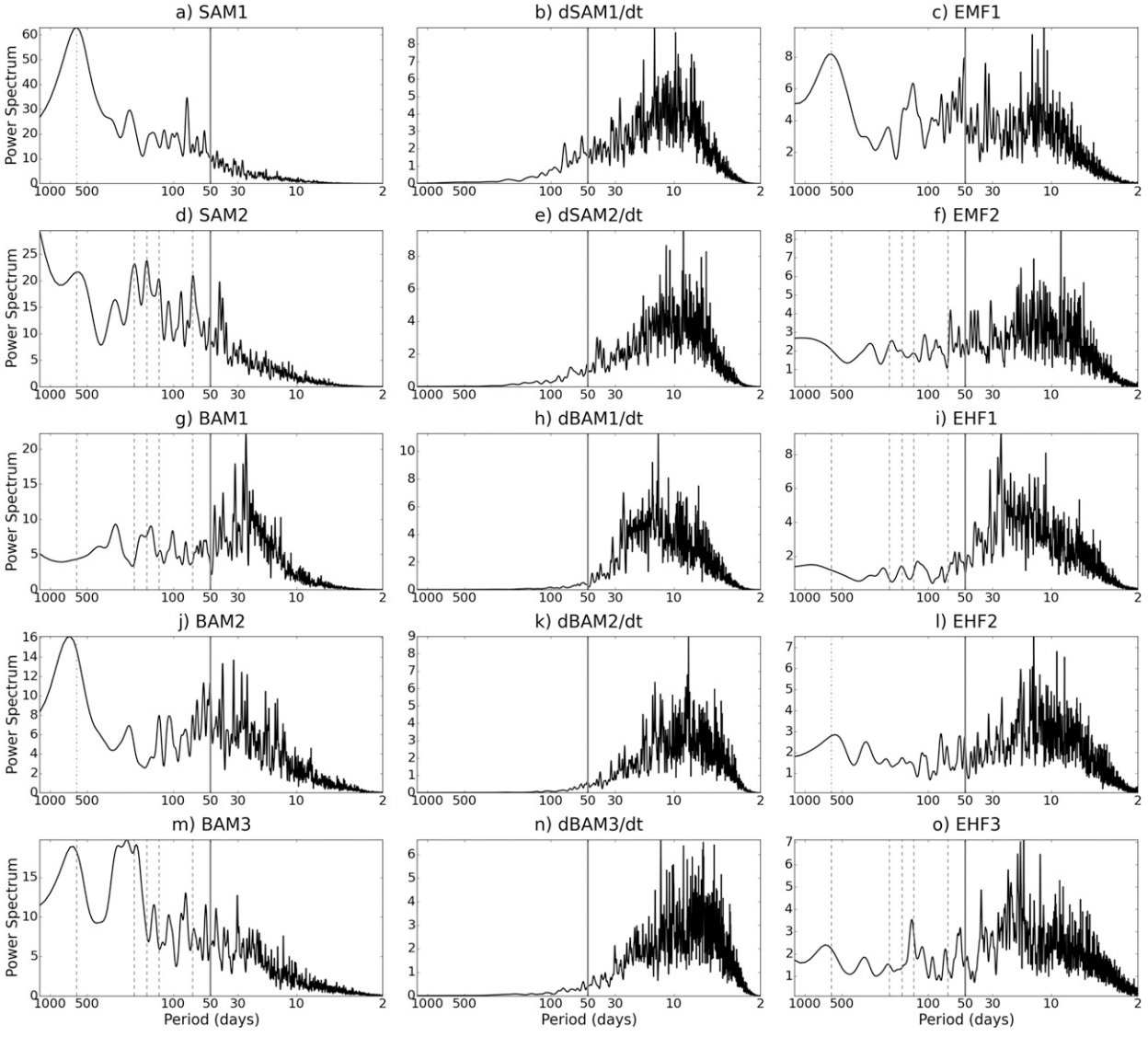

FIG. 9. As in Fig. 4, but for ERA-Interim.

intermediate time scales. The EKE damping time scale τ_{EKE} varies between 1.5 and 4.2 days, while the parameter $|\alpha_{\mathrm{EKE}}|$ varies between 5.6 and 11.4 $\times$ $10^{-5}\,\mathrm{m\,K^{-1}\,s^{-2}}$. While τ_{EKE} is consistent with the value found in Thompson et al. (2017), $|\alpha_{\mathrm{EKE}}|$ is larger. This is because Thompson et al. (2017) regressed the tendency of EKE onto the heat flux to calculate $|\alpha_{\mathrm{EKE}}|$, and the former is dominated by higher frequencies (as shown through power spectra; e.g., Fig. 4), whereas here, we calculate it for periods longer than 10 days where relationship (6) is robust, and the EKE, not its tendency, is used for calculations.

Figures 7–9 show the power spectra for the winter and summer model configurations and for ERA-Interim (with the same panels as in Fig. 4). These power spectra imply robust relationships between SAM and EMF modes, and between BAM and EHF modes, at all frequency ranges, according to (4) and (6), respectively. BAM1 and EHF1 exhibit power in the intermediate frequency range, for which the cross spectra showed a decoupling from the barotropic dynamics, whereas the rest of the modes exhibit the synoptic time scale (around 10-day periods) and quasi-steady (periods much longer than 50 days) behavior. While the links between SAM and EMF modes and between BAM and EHF modes follow from the theory presented in section 3, the links between the SAMs and BAMs are nontrivial. To elucidate these links, the correlations between different SAMs and BAMs are given in Tables 2–4 to complement the power spectra in Figs. 4 and 7–9.

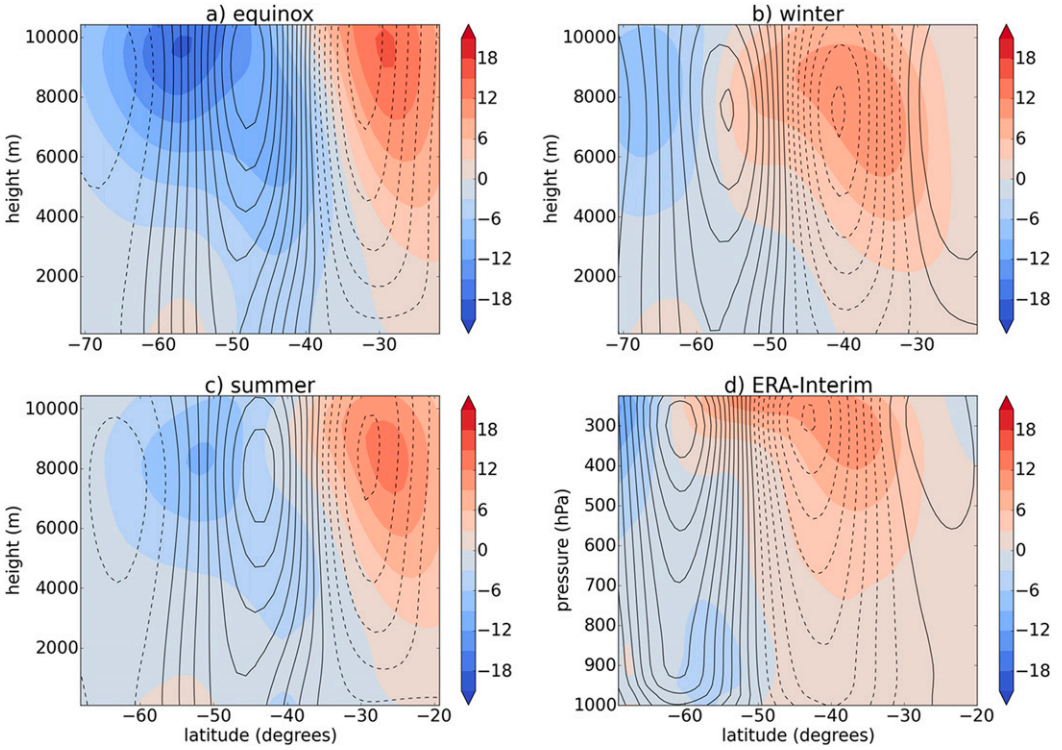

FIG. 10. Regressions of high-pass EKE (shading; $m^2\,s^{-2}$) and high-pass zonal-mean zonal wind (contours; $m\,s^{-1}$) on high-pass SAM1 for (a) equinox, (b) winter, and (c) summer model configurations and (d) ERA-Interim. The contour interval is $0.3\,m\,s^{-1}$ ($\ldots, -0.3, 0, 0.3, 0.6, \ldots\,m\,s^{-1}$). The dashed lines represent negative values, and solid lines represent positive values.

The high-pass data in Tables 2 and 3 show robust negative correlations between the SAM1 and BAM2 modes, and between the SAM2 and BAM1 modes, respectively. This seems broadly consistent with TEM theory. Since $\partial[u]/\partial t$ is proportional to $\nabla \cdot \mathbf{F}$ [e.g., (2.3a) in Edmon et al. (1980)] and $\partial[K_E]/\partial t$ is proportional to $-\nabla \cdot \mathbf{F}$ [(2); note that $[u]$ is generally westerly in the midlatitudes and hence does not affect the sign of the correlations], a negative correlation between corresponding SAMs and BAMs is expected on synoptic time scales as the tendencies reflect the high-frequency behavior (as seen from the power spectra). SAM1 is a dipolar mode and thus matches BAM2. Although SAM2 is a tripolar mode and therefore might be expected to match BAM3, the correlation between SAM2 and BAM3 at high frequencies (Table 4) is nonrobust or even negligible. Instead, SAM2 is negatively correlated with BAM1, which projects onto the center of SAM2. These negative correlations between SAM1 and BAM2 and between SAM2 and BAM1 are further confirmed in Figs. 10 and 11, where the regressions of high-pass EKE (shading) on high-pass SAMs tend to exhibit the opposite sign to high-pass $[u]$ (contours) regressions on the same modes.

The low-pass data in Tables 2 and 4 show robust positive correlations between the SAM1 and BAM2 modes, and between the SAM2 and BAM3 modes, respectively, consistent with the quasi-steady positive baroclinic feedback (Robinson 2000) described in section 4b. Moreover, there is a clear correspondence between the SAM1 and BAM2, and between the SAM2 and BAM3 low-frequency spectral peaks in all cases (Figs. 4, 7–9). Figures 12 and 13 further show that the regression of low-pass EKE on low-pass SAM1 and SAM2 reflects BAM2- and BAM3-like behavior, respectively, and that positive SAMs are related to positive BAMs (i.e., positive wind anomaly is associated with positive EKE anomaly, indicating a storm-track shift with the jet stream, a positive baroclinic feedback mechanism), consistent with the correlations. Figures S3 and S4 in the supplementary material also show that the spatial structures of SAM1 and BAM2, and of SAM2 and BAM3, for all model configurations and for ERA-Interim are in phase; that is, the major peaks in the SAMs and BAMs closely follow each other.

On the other hand, the low-pass correlations between SAM2 and BAM1 are nonrobust (Table 3), and there is no clear correspondence between their low-frequency spectral peaks (Figs. 4, 7–9). This implies

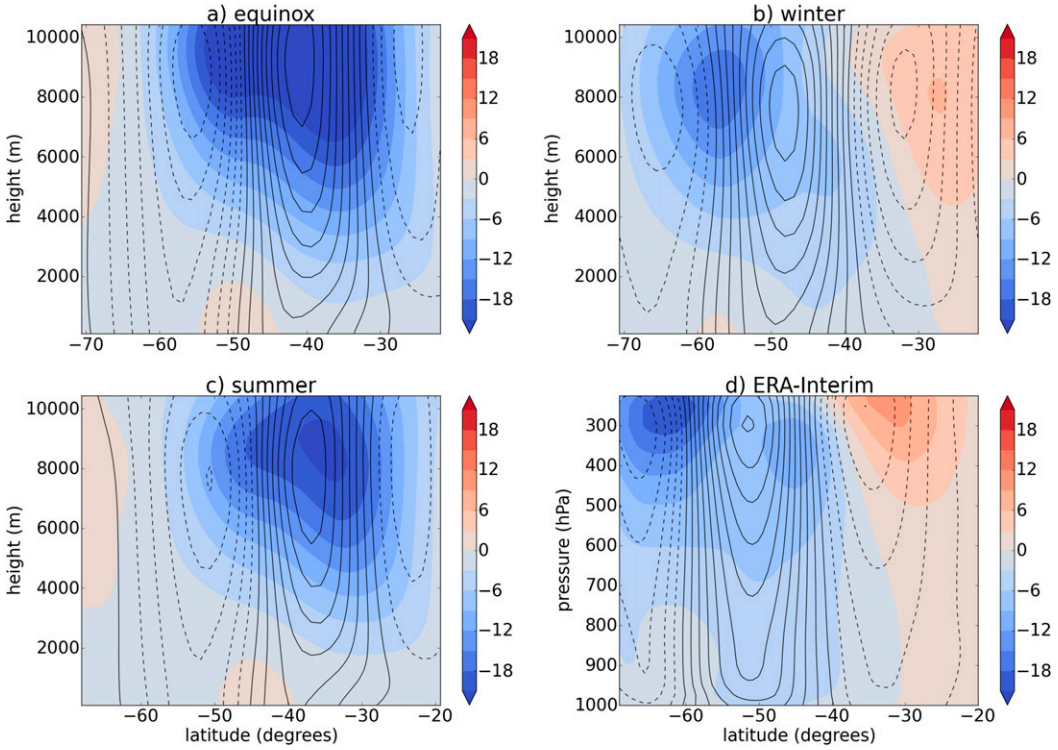

FIG. 11. As in Fig. 10, but for the regressions on high-pass SAM2.

that any link between SAM2 and BAM1 is state dependent. This is further demonstrated in Fig. S4, which shows the spatial structures of SAM2 and BAM1. While it is clear from this figure that the main peaks in SAM2 and BAM1 for ERA-Interim are in phase and could explain the high correlation between the two modes, it is less clear for the model configurations. The winter configuration shows a high correlation between SAM2 and BAM1; however, the spatial structures are out of phase, suggesting that the high correlation could be a consequence of the chosen cutoff period (50 days) as in this case the BAM1 power spectrum peaks around 50 days (Fig. 7).

The correlations for the unfiltered data reflect the combination of high- and low-frequency behavior. This is especially true for SAM1 and BAM2 (Table 2), where the unfiltered correlations are dominated by the low frequencies; however, the weaker correlations in the unfiltered case suggest the influence of the negative high-frequency correlations [consistent with Sparrow et al. (2009)]. Figure 14 further demonstrates this through a much lower correlation at zero lags, which increases at positive and negative lags (approximately ±5 days). Thus, the negative high-frequency correlations depress the correlations at short time lags. This behavior also explains the negative correlation between SAM1 and BAM2 for ERA-Interim at zero lag. Table 4 shows that the unfiltered correlations between SAM2 and BAM3 are dominated by low-frequency behavior. In contrast, Table 3 shows that the unfiltered correlations between SAM2 and BAM1 for the equinox and summer model configurations are dominated by the high-frequency behavior, whereas for the winter model configuration and ERA-Interim, a combination of low- and high-frequency behavior is reflected in the unfiltered correlations. Note also that SAM1 and SAM2 can exhibit significant correlations at nonzero lags, especially for the winter configuration where the separation of modes is smaller (Sheshadri and Plumb 2017; note that they used the same winter and summer model configurations as used here). Hence, SAM1 and SAM2 could together represent propagating modes of variability and should not necessarily be considered separately (Sparrow et al. 2009; Sheshadri and Plumb 2017). Examining the low-frequency spectral peaks is a way to determine whether there is covariability of SAM1 and SAM2.

6. Summary and conclusions

This study has investigated the coupling between the baroclinic (BAM) and barotropic (SAM) modes of variability using power- and cross-spectrum analyses, regressions, and correlations in different Held–Suarez model configurations and in ERA-Interim SH datasets.

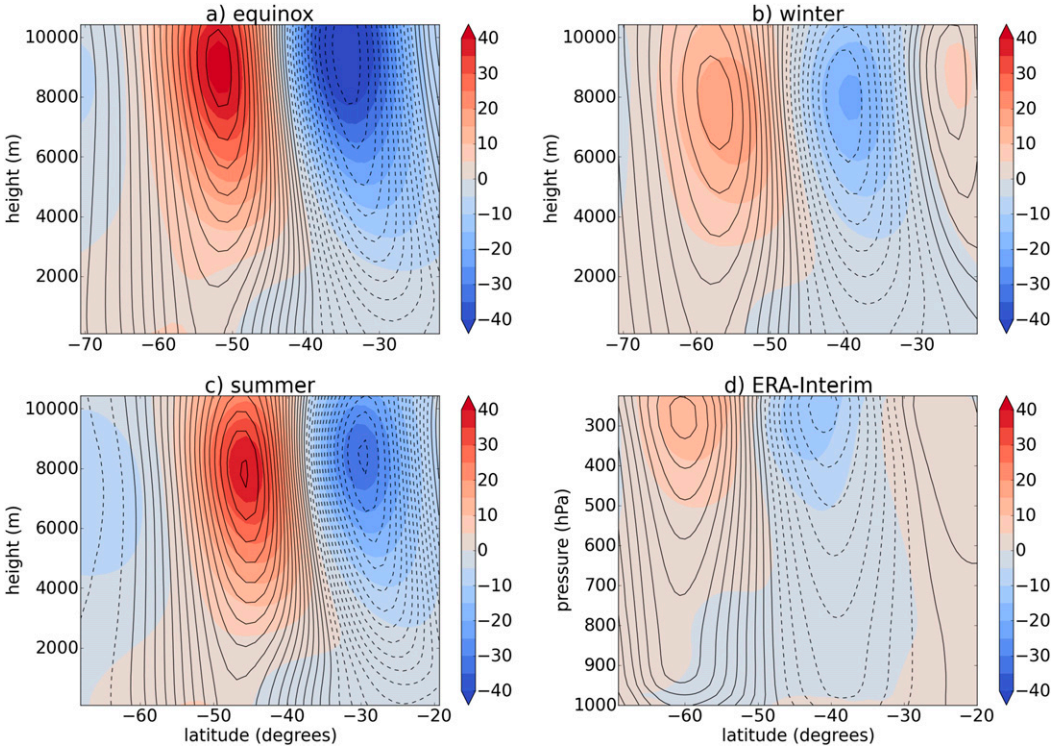

FIG. 12. Regressions of low-pass EKE (shading; $m^2\,s^{-2}$) and low-pass zonal-mean zonal wind (contours; $m\,s^{-1}$) on low-pass SAM1 for (a) equinox, (b) winter, and (c) summer model configurations and (d) ERA-Interim. The contour interval is $0.3\,m\,s^{-1}$ ($\ldots, -0.3, 0, 0.3, 0.6, \ldots\,m\,s^{-1}$). The dashed lines represent negative values, and solid lines represent positive values.

We have shown through the cross-spectrum analysis that there is a robust relationship across time scales between EKE and eddy heat fluxes [(6)], analogous to that between zonal-mean zonal wind and eddy momentum flux convergence [(4); Lorenz and Hartmann 2001]. However, the former relationship is weaker as it fails for periods shorter than about 10 days, and the quasi-steady balance between EKE and heat flux is nonnegligible at intermediate time scales [at least for periods longer than 20 days, consistent with the oscillator model of Thompson and Barnes (2014)]. This is a consequence of a robustly shorter damping time scale on EKE ($\tau_{\mathrm{EKE}} \approx 3$ days) compared to the zonal-mean zonal wind damping time scale ($\tau \approx 10$ days) and is reflected in the reduced curvature of the phase difference plot in Fig. 3a(ii) compared with Fig. 2b. The weaker relationship between EKE and heat flux is understandable because of the presence of additional terms in the EKE equation [see (2)]; moreover, asymptotic theory (Boljka and Shepherd 2018) shows that one needs to average over the synoptic temporal and spatial scales to obtain this relationship. A stronger relationship might be possible using wave activity instead of EKE; this is left for future work.

These cross-spectra relationships suggest a proximate link between zonal-mean zonal wind and eddy momentum flux only [(4)] and between EKE and eddy heat flux only [(6)], recognizing that the eddies are themselves baroclinic. The latter link is consistent with a decoupling of the baroclinic (BAM) from the barotropic (SAM) modes of variability [as in Thompson and Woodworth (2014)], at least at periods longer than 10 days, as predicted by the asymptotic model for intermediate time scales (i.e., not for quasi-steady state).

The frequency power spectra of eddy momentum and heat fluxes reveal that they generally exhibit a broad peak at higher frequencies (<30-day periods), as well as distinct peaks at lower frequencies (>50-day periods). The higher-frequency eddy fluxes are related to the tendencies of EKE and of zonal-mean zonal wind (i.e., $\partial z_u/\partial t \approx m$ and $\partial[K_E]/\partial t \approx \alpha_{\mathrm{EKE}}[v^*\theta^*]$), whereas the lower-frequency peaks relate to the quantities themselves (EKE or zonal-mean zonal wind; i.e., $z_u/\tau \approx m$ and $[K_E]/\tau_{\mathrm{EKE}} \approx \alpha_{\mathrm{EKE}}[v^*\theta^*]$). This was indeed confirmed by the cross-spectrum analysis as mentioned above.

There is a direct quasi-steady relationship between EMF and SAM and between EHF and BAM, which applies mode by mode, as can be seen through direct

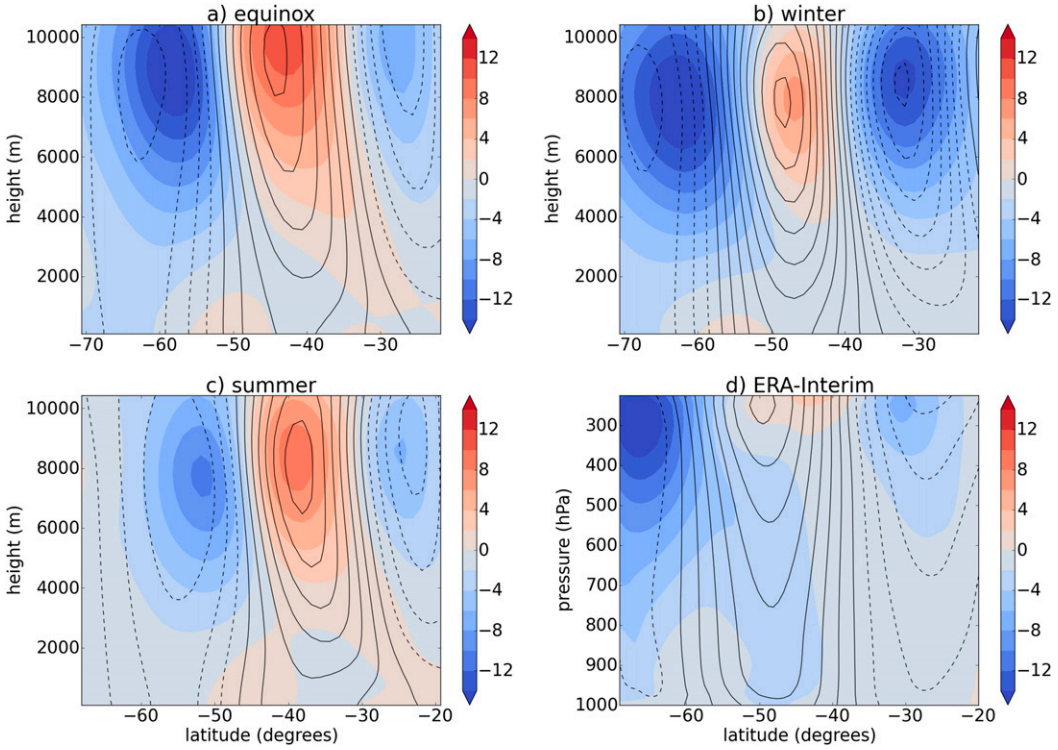

FIG. 13. As in Fig. 12, but for the regressions on low-pass SAM2. Note that the color scale was adjusted to the values of EKE regression on this mode.

matching of low-frequency peaks in the power spectra and is seen in all model configurations and in ERA-Interim. There are also cross-mode relationships at quasi-steady state. There is a robust positive relation between SAM1 and BAM2 (shifted jet and storm track) and between SAM2 and BAM3 (strengthened jet and storm track), reflecting a positive baroclinic feedback (Robinson 2000). The relationships between SAM2 and BAM1 are less robust and depend on model climatology and variability. These relationships could be the subject of future investigations but can be expected to be state dependent. We find no evidence of a cross-mode relationship between SAM1 and BAM1, which was the correlation examined by Thompson and Woodworth (2014).

There are also cross-mode relationships in high-pass data, which are more complex (reflecting transient wave–mean flow interaction and baroclinic life cycles) and tend to be of opposite sign to those at lower frequencies. Thus, combining low- and high-pass data leads to a confusing picture as it combines different kinds of behavior that can exhibit some cancellation between them [as shown by Sparrow et al. (2009)].

In summary, this study has shown that the nature and extent of the coupling between barotropic and baroclinic modes of extratropical atmospheric variability depend strongly on the time scale of variability. On synoptic time scales, there is negative coupling through the baroclinic life cycle (Simmons and Hoskins 1978); on quasi-steady time scales (periods longer than 50 days), there is positive coupling through the baroclinic feedback mechanism

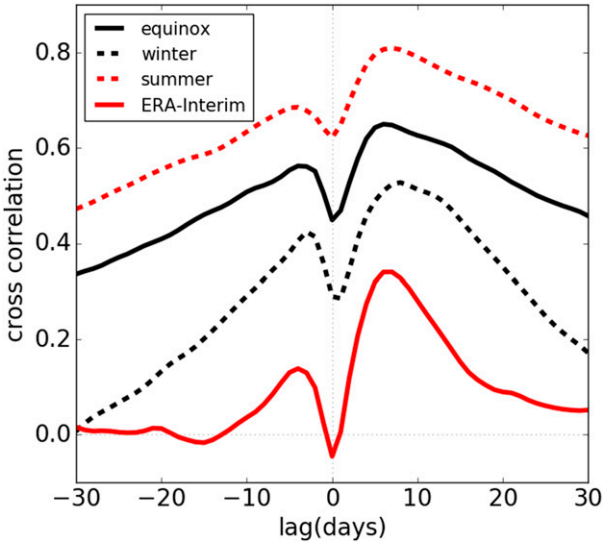

FIG. 14. Lagged correlations between SAM1 and BAM2 (unfiltered) for equinox (black solid), winter (black dashed), and summer (red dashed) model configurations and ERA-Interim (red solid).

(Robinson 2000); and on intermediate time scales, there is a decoupling, with purely baroclinic variability that can manifest itself in a baroclinic oscillator (Thompson and Barnes 2014), consistent with weakly nonlinear models of baroclinic instability (Pedlosky 1970). In the quasi-steady limit, the pulsating modes of variability and their correlations depend sensitively on the model climatology. This could have implications for the modeled circulation response to climate change.

Acknowledgments. This work was funded by the European Research Council (Advanced Grant ACRCC, "Understanding the atmospheric circulation response to climate change" Project 339390). We thank the three anonymous reviewers for their comments, which helped improve the original manuscript. We acknowledge Nick Byrne, Aditi Sheshadri, Simon Peatman, Tom Frame, Clare Watt, Chris Smith (Met Office), and NCAS-CMS for help and discussions. This work used the ARCHER U.K. national supercomputing service and the U.K. research data facility (http://www.archer.ac.uk). We also thank the Met Office for the use of its Unified Model. The model data can be reproduced using the Unified Model (details and scripts are available upon request).

REFERENCES

Ambaum, M. H. P., and L. Novak, 2014: A nonlinear oscillator describing storm track variability. *Quart. J. Roy. Meteor. Soc.*, **140**, 2680–2684, https://doi.org/10.1002/qj.2352.

Andrews, D. G., and M. E. McIntyre, 1976: Planetary waves in horizontal and vertical shear: The generalized Eliassen-Palm relation and the mean zonal acceleration. *J. Atmos. Sci.*, **33**, 2031–2048, https://doi.org/10.1175/1520-0469(1976)033<2031:PWIHAV>2.0.CO;2.

Bloomfield, P., 2000: *Fourier Analysis of Time Series: An Introduction.* Wiley, 286 pp.

Boljka, L., and T. G. Shepherd, 2018: A multiscale asymptotic theory of extratropical wave–mean flow interaction. *J. Atmos. Sci.*, **75**, 1833–1852, https://doi.org/10.1175/JAS-D-17-0307.1.

Byrne, N. J., T. G. Shepherd, T. Woollings, and R. A. Plumb, 2016: Annular modes and apparent eddy feedbacks in the Southern Hemisphere. *Geophys. Res. Lett.*, **43**, 3897–3902, https://doi.org/10.1002/2016GL068851.

Dee, D. P., and Coauthors, 2011: The ERA-Interim reanalysis: Configuration and performance of the data assimilation system. *Quart. J. Roy. Meteor. Soc.*, **137**, 553–597, https://doi.org/10.1002/qj.828.

Duchon, C. E., 1979: Lanczos filtering in one and two dimensions. *J. Appl. Meteor.*, **18**, 1016–1022, https://doi.org/10.1175/1520-0450(1979)018<1016:LFIOAT>2.0.CO;2.

Edmon, H. J., B. J. Hoskins, and M. E. McIntyre, 1980: Eliassen-Palm cross sections for the troposphere. *J. Atmos. Sci.*, **37**, 2600–2616, https://doi.org/10.1175/1520-0469(1980)037<2600:EPCSFT>2.0.CO;2; Corrigendum, **38**, 1115, https://doi.org/10.1175/1520-0469(1981)038<1115:>2.0.CO;2.

Hartmann, D. L., and F. Lo, 1998: Wave-driven zonal flow vacillation in the Southern Hemisphere. *J. Atmos. Sci.*, **55**, 1303–1315, https://doi.org/10.1175/1520-0469(1998)055<1303:WDZFVI>2.0.CO;2.

Haynes, P. H., and T. G. Shepherd, 1989: The importance of surface pressure changes in the response of the atmosphere to zonally-symmetric thermal and mechanical forcing. *Quart. J. Roy. Meteor. Soc.*, **115**, 1181–1208, https://doi.org/10.1002/qj.49711549002.

Held, I. M., and M. J. Suarez, 1994: A proposal for the intercomparison of the dynamical cores of atmospheric general circulation models. *Bull. Amer. Meteor. Soc.*, **75**, 1825–1830, https://doi.org/10.1175/1520-0477(1994)075<1825:APFTIO>2.0.CO;2.

Kidson, J. W., 1988: Indices of the Southern Hemisphere zonal wind. *J. Climate*, **1**, 183–194, https://doi.org/10.1175/1520-0442(1988)001<0183:IOTSHZ>2.0.CO;2.

Lorenz, D. J., and D. L. Hartmann, 2001: Eddy–zonal flow feedback in the Southern Hemisphere. *J. Atmos. Sci.*, **58**, 3312–3327, https://doi.org/10.1175/1520-0469(2001)058<3312:EZFFIT>2.0.CO;2.

Pedlosky, J., 1970: Finite-amplitude baroclinic waves. *J. Atmos. Sci.*, **27**, 15–30, https://doi.org/10.1175/1520-0469(1970)027<0015:FABW>2.0.CO;2.

Pfeffer, R. L., 1987: Comparison of conventional and transformed Eulerian diagnostics in the troposphere. *Quart. J. Roy. Meteor. Soc.*, **113**, 237–254, https://doi.org/10.1256/smsqj.47513.

——, 1992: A study of eddy-induced fluctuations of the zonal-mean wind using conventional and transformed Eulerian diagnostics. *J. Atmos. Sci.*, **49**, 1036–1050, https://doi.org/10.1175/1520-0469(1992)049<1036:ASOEIF>2.0.CO;2.

Plumb, R. A., 1983: A new look at the energy cycle. *J. Atmos. Sci.*, **40**, 1669–1688, https://doi.org/10.1175/1520-0469(1983)040<1669:ANLATE>2.0.CO;2.

Polvani, L. M., and P. J. Kushner, 2002: Tropospheric response to stratospheric perturbations in a relatively simple general circulation model. *Geophys. Res. Lett.*, **29**, 1114, https://doi.org/10.1029/2001GL014284.

Robinson, W. A., 2000: A baroclinic mechanism for the eddy feedback on the zonal index. *J. Atmos. Sci.*, **57**, 415–422, https://doi.org/10.1175/1520-0469(2000)057<0415:ABMFTE>2.0.CO;2.

Sheshadri, A., and R. A. Plumb, 2017: Propagating annular modes: Empirical orthogonal functions, principal oscillation patterns, and time scales. *J. Atmos. Sci.*, **74**, 1345–1361, https://doi.org/10.1175/JAS-D-16-0291.1.

——, ——, and E. P. Gerber, 2015: Seasonal variability of the polar stratospheric vortex in an idealized AGCM with varying tropospheric wave forcing. *J. Atmos. Sci.*, **72**, 2248–2266, https://doi.org/10.1175/JAS-D-14-0191.1.

Simmons, A. J., and B. J. Hoskins, 1978: The life cycles of some nonlinear baroclinic waves. *J. Atmos. Sci.*, **35**, 414–432, https://doi.org/10.1175/1520-0469(1978)035<0414:TLCOSN>2.0.CO;2.

Sparrow, S., M. Blackburn, and J. D. Haigh, 2009: Annular variability and eddy–zonal flow interactions in a simplified atmospheric GCM. Part I: Characterization of high- and low-frequency behavior. *J. Atmos. Sci.*, **66**, 3075–3094, https://doi.org/10.1175/2009JAS2953.1.

Thompson, D. W. J., and E. A. Barnes, 2014: Periodic variability in the large-scale Southern Hemisphere atmospheric circulation. *Science*, **343**, 641–645, https://doi.org/10.1126/science.1247660.

——, and J. D. Woodworth, 2014: Barotropic and baroclinic annular variability in the Southern Hemisphere. *J. Atmos. Sci.*, **71**, 1480–1493, https://doi.org/10.1175/JAS-D-13-0185.1.

——, B. R. Crow, and E. A. Barnes, 2017: Intraseasonal periodicity in the Southern Hemisphere circulation on regional spatial scales. *J. Atmos. Sci.*, **74**, 865–877, https://doi.org/10.1175/JAS-D-16-0094.1.

Thorncroft, C. D., B. J. Hoskins, and M. E. McIntyre, 1993: Two paradigms of baroclinic-wave life-cycle behaviour. *Quart. J. Roy. Meteor. Soc.*, **119**, 17–55, https://doi.org/10.1002/qj.49711950903.

Vallis, G. K., E. P. Gerber, P. J. Kushner, and B. A. Cash, 2004: A mechanism and simple dynamical model of the North Atlantic Oscillation and annular modes. *J. Atmos. Sci.*, **61**, 264–280, https://doi.org/10.1175/1520-0469(2004)061<0264:AMASDM>2.0.CO;2.

Walters, D., N. Wood, S. Vosper, and S. Milton, 2014: ENDGame: A new dynamical core for seamless atmospheric prediction. Met Office Tech. Rep., 30 pp.

Wang, L., and N. Nakamura, 2015: Covariation of finite-amplitude wave activity and the zonal mean flow in the midlatitude troposphere: 1. Theory and application to the Southern Hemisphere summer. *Geophys. Res. Lett.*, **42**, 8192–8200, https://doi.org/10.1002/2015GL065830.

——, and ——, 2016: Covariation of finite-amplitude wave activity and the zonal-mean flow in the midlatitude troposphere. Part II: Eddy forcing spectra and the periodic behavior in the Southern Hemisphere summer. *J. Atmos. Sci.*, **73**, 4731–4752, https://doi.org/10.1175/JAS-D-16-0091.1.